PHYSICAL REVIEW B **108**, 235211 (2023)

Complete topological phase diagram and realization of minimum Weyl nodes in a sheared chiral crystal of elemental tellurium

Shuai Fan,[1] Botao Fu,[2] Da-Shuai Ma,[1,3,*] and Rui Wang[1,3,†]

[1]*Institute for Structure and Function & Department of Physics & Chongqing Key Laboratory for Strongly Coupled Physics, Chongqing University, Chongqing 400044, People's Republic of China*

[2]*College of Physics and Electronic Engineering, Center for Computational Sciences, Sichuan Normal University, Chengdu, 610068, People's Republic of China*

[3]*Center of Quantum Materials and Devices, Chongqing University, Chongqing 400044, People's Republic of China*

(Received 26 September 2023; accepted 11 December 2023; published 26 December 2023)

Ideal Weyl semimetals, with minimum Weyl nodes located far away from each other in reciprocal space and near the Fermi level in the energy space, are considered to be crucial for revealing the intrinsic physical properties of Weyl semimetals. Based on first-principles calculations, we demonstrate that elemental tellurium, under application of a broad range of shear strain, is a candidate for realizing ideal Weyl semimetals. Particularly, the sheared elemental tellurium has only four Weyl nodes in the Brillouin zone, which is the minimum number of Weyl nodes that can be achieved by a system with time-reversal symmetry. More importantly, by adjusting the strength of the strain, we obtain abundant topological phases, i.e., Weyl semimetals, strong topological insulators, composite Weyl semimetals, and weak topological insulators in elemental tellurium. Notably, this paper proposes implementing a weak topological insulator phase in a space group with only time-reversal symmetry. The complete topological phase diagram of sheared tellurium is given and the topological properties of different topological nontrivial phases are characterized, respectively.

DOI: 10.1103/PhysRevB.108.235211

I. INTRODUCTION

Weyl semimetals (WSMs), three-dimensional (3D) crystals characterized by the topological properties of the zero-dimensional crossing manifold of band structure in the bulk Brillioun zone (BZ), have grasped extensive attention in the past decade [1–10]. Physically, Weyl points work as a source or a sink of the Berry curvature in the BZ, which requires the breaking time-reversal symmetry or inversion symmetry. The nontrivial band topology of the zero-dimensional band crossing is characterized by the quantized integration of the Berry curvature on a surface that encloses the node point, i.e., chirality. According to the Nielsen-Ninomiya no-go theorem, chiralities of Weyl nodes throughout the BZ sum to zero [11–13]. A variety of intriguing properties such as topologically protected surface states, i.e., open Fermi arcs [1,4,14–19], chiral anomaly effect [20–25], the negative longitudinal resistance [26–28], and prominent anomalous Hall effect [29–34] have been reported in WSMs. Some WSMs have been proposed theoretically and confirmed experimentally. Nevertheless, in previous proposed crystals, systems often possess too many chemical elements and Weyl nodes, and some Weyl nodes locate near each other [35–40]. Moreover, in many previous reports, WSM candidate systems have encountered difficulties in practical applications due to the involvement of environmentally unfriendly elements such as As. All of the disadvantages imply that searching for the ideal WSM with a simple crystal structure and the minimum number of Weyl nodes that separate to each other is still desirable for research focused on the intrinsic physical properties of Weyl fermions.

Elemental tellurium (Te), a quasi-one-dimensional van der Waals material consisting of characteristic chiral helical chains [see Figs. 1(a)–1(b)] [41], has exhibited many intriguing physical properties such as multiferroic behavior [42], piezoelectric effect [43], high-efficiency thermoelectricity [44–46], and high hole mobilities [47]. The weak interchain interaction suggests it is possible to exfoliate Te into ultrathin films and nanowires, which is verified by many recent experimental works and attracts plenty of attention [48–52]. Note that, due to the characteristic crystal structure, strain is regarded as a highly feasible means to engineer the electronic and topological properties of Te [53–55]. In fact, some topological nontrivial properties were reported in Te with/without strain already. Specifically, under application of hydrostatic pressure, Te turns into a WSM, which is one of the earliest theoretical works that realize Weyl fermion in systems without inversion symmetry [54]. Notably, this prediction has recently been experimentally verified [55,56]. Moreover, by angle-resolved photoemission spectroscopy and density functional theory (DFT), in the valance bands of Te, Weyl nodes were found [57–59], whereas, guaranteed by the high symmetry, too many Weyl nodes were found to coexist in Te. On the other hand, Te is stated to be a strong topological insulator (STI) with shear strain [53]. However, a complete topological phase diagram of elemental tellurium under shear strain is still lacking and desired. For example, due to the

---

[*] madason.xin@gmail.com

[†] rcwang@cqu.edu.cn

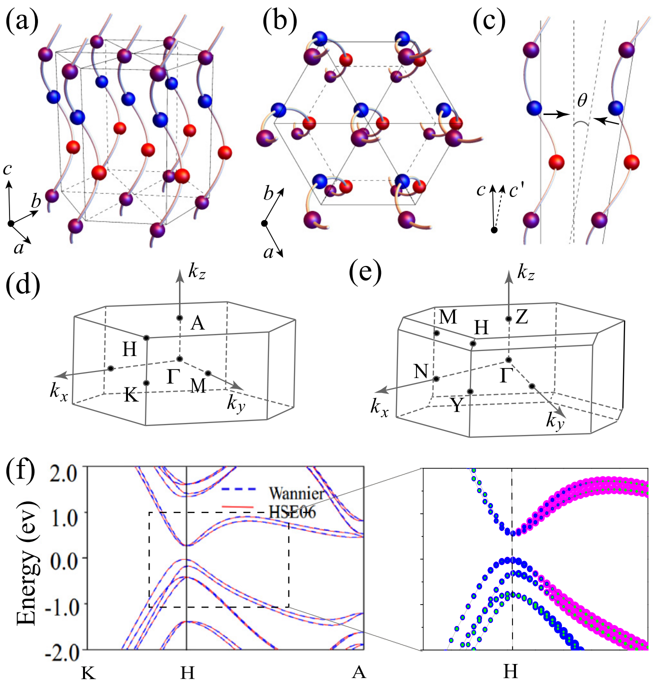

FIG. 1. (a) Side view and (b) top view of the crystal structure of elemental Te. Here, the balls in purple, red, and blue represent the three unequal Te atoms in the unit cell, respectively. (c) Schematic diagram of the shear strain that induced by tilt the chiral helical chain θ radian towards [110] direction. (d), (e) Bulk Brillouin zone of Te (d) and sheared Te (e). (f) The band structures of Te calculated by HSE06 and WLWF. The weights of the p_x, p_y, and p_z orbits of Te are highlighted in blue, purple, and green, respectively, in the right panel.

absence of inversion symmetry [60], the Weyl phase must appear during the phase transition from normal insulator (NI) to STI.

In this paper, based on first-principles calculations, we present a comprehensive investigation on the electronic and topological properties of tellurium with shear strain. We demonstrate that, during the NI-STI phase transition, elemental Te becomes a WSM. In sharp contrast to the WSM phase revealed in Te with hydrostatic pressure, the sheared Te, with lower symmetry, possesses the minimum Weyl nodes, i.e., two pairs for systems with time-reversal symmetry. Remarkably, the four Weyl nodes are far apart from each other in the BZ, which effectively avoids the scattering effect among Weyl nodes. Moreover, we give the complete topological phase diagram of Te under shear strain. With the increasing strength of strain, abundant topological nontrivial phases are found. For each topological phase, the topological properties are characterized by the topological invariant and surface states, respectively.

II. CRYSTAL STRUCTURE AND METHODOLOGY

Tellurium is well-known as a chiral crystal. As shown in Figs. 1(a)–1(c), each unit cell of Te is made up of three nonequivalent Te atoms. These three atoms are periodically stacked in an orderly fashion along the c axis, forming a chiral helical chain, as shown in see Figs. 1(a)–1(c). Consisting of parallel right-/left-handed helical chains, Te belongs to the $P3_121\text{-}D_3^4/P3_221\text{-}D_3^6$ space group (No. 152/No. 154) with trigonal structure. The crystal structure of the right-handed elemental Te is shown in Figs. 1(a)–1(c). It is worth noting that since there is no difference in the electronic properties of right-handed and left-handed Te, we focus on right-handed Te hereafter.

The first-principles calculations were performed within the framework of DFT [61,62] with the projector augmented wave method [63,64], as implemented in the Vienna Ab initio Simulation Package (VASP) [65,66]. The band structures are obtained by employing the nonlocal HeydScuseria-Ernzerhof (HSE06) hybrid functional method [67]. A tested Γ-centered k-mesh 7 × 7 × 5 was used to sample the Brillouin zone (BZ). The kinetic energy cutoff for the plane-wave basis was set as 300 eV. The experimental lattice parameters, $a = b = 4.45$ Å and $c = 5.93$ Å, were used in all these calculations [68]. Under each strain, the atom positions are fully relaxed. The maximally localized Wannier functions (MLWFs) projected from the bulk Bloch wave functions were constructed to obtain the tight-binding Hamiltonian [69–73]. The iterative Green's function method as implemented in WANNIERTOOLS [74] was used for calculation of the topological surface states and Fermi arcs.

III. THE ELECTRONIC PROPERTIES OF TE

The band structure of Te without strain is shown in Fig. 1(f). With a Rashba-like spin splitting, the edges of both conduction and valence bands are pinned near the high-symmetry point H: (1/3, 1/3, 1/2) of the bulk BZ, which indicates that Te is an insulator with a narrow indirect band gap. The band gap of Te calculated by HSE06 method is 0.295 eV, as shown in Fig. 1(f). The calculated band gap is in good agreement with the value 0.323 eV measured under the low experimental temperature 4.2 K [75,76] and the theoretical value 0.314 eV given by the *GW* correction [54]. Further, we performed the orbital-resolved calculation, as shown in the right panel of Fig. 1(f). The band-project analysis demonstrates that the bands near the Fermi level are mainly contributed by the p orbits of Te. Hence, in further calculation, the MLWFs are only constructed for the p orbits, and a highly accordant energy spectrum with the DFT result is obtained and shown Fig. 1(f).

IV. THE TOPOLOGICAL PHASE DIAGRAM
OF TE UNDER SHEAR STRAIN

Now we apply finite shear strain along the [110] direction. Concretely, for the first-principles calculations, we tilt the c axis towards the [110] direction to the c' axis, as schematically shown in Fig. 1(c). The strength of the shear strain is defined as

$$\varepsilon = 2\frac{\theta}{\pi} \times 100\%, \tag{1}$$

with the parameter θ being the angle between the c axis and the tilted c' axis, as shown in Fig. 1(c). For all the chiral helical chains being tilted, the crystal structure of Te turns to the

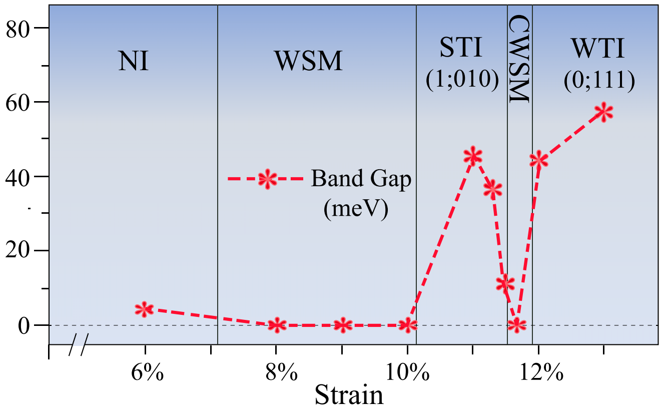

FIG. 2. The topological phase diagram of Te under application of shear strain. The minimum local band gap of sheared Te, in units of meV, varying with the strength of shear strain, is shown by the dashed line in red.

chiral triclinic structure that belongs to the $P1$ space group (No. 1). This space group has the lowest crystal symmetry, only the identity symmetry, which helps reveal WSMs that possess the fewest Weyl nodes.

With the strength of strain increasing, the local band gap of Te presents a rich variation, corresponding to abundant topological phases, shown in Fig. 2. The narrow band gap of Te decreases from 0% ~ 7% shear strain, and the system keeps a topological trivial insulator phase. At ≈7.5% shear strain, the energy gap of Te vanishes, resulting in the emergence of a WSM phase. Under the application of a stronger strain (8% ~ 10%), sheared Te remains a semimetal phase. Weyl nodes in sheared Te annihilate at ≈10.5% and appear near ≈11.6% strain again. In sharp contrast to the WSM phase in the range of 8% ~ 10%, the ≈11.6% sheared Te is a composite Weyl semimetal (CWSM) phase, which is characterized by the coexist of the surface arc and circle in the isoenergy band contours of certain surface band [77]. An increasing band gap appears in Te under application of shear strain ⩾ 12%. In fact, at 10.5% ~ 11.5% and ⩾ 12% shear strain, Te is a STI and weak topological insulator (WTI), respectively. Notably, the bottom (top) of the conduction (valance) band is pulled down (up) toward and cross the Fermi level. Thus, as discussed in later sections, the system becomes a metal phase with local band gap, i.e., a topological metal.

V. WEYL SEMIMETAL PHASE IN SHEARED TE

Now, we first demonstrate that, under application of 10% shear strain, Te is revealed to be an ideal WSM with minimal Weyl nodes. The band structure of 10% sheared Te is shown in Fig. 3(a). It is observable that there is still a local gap along the line with high symmetry in BZ. However, at general points in the bulk BZ, there may be some gapless points, i.e., Weyl nodes. With more precise band calculations, we find two gapless points at ±(0.4690, −0.1628, 0.3528) (these coordinates are written under the reciprocal lattice vector as basis), labeled W_1 and W_2, respectively. Since two Weyl nodes are connected to each other by time-reversal symmetry, they carry the same chirality, i.e., the Chern number calculated to be −1.

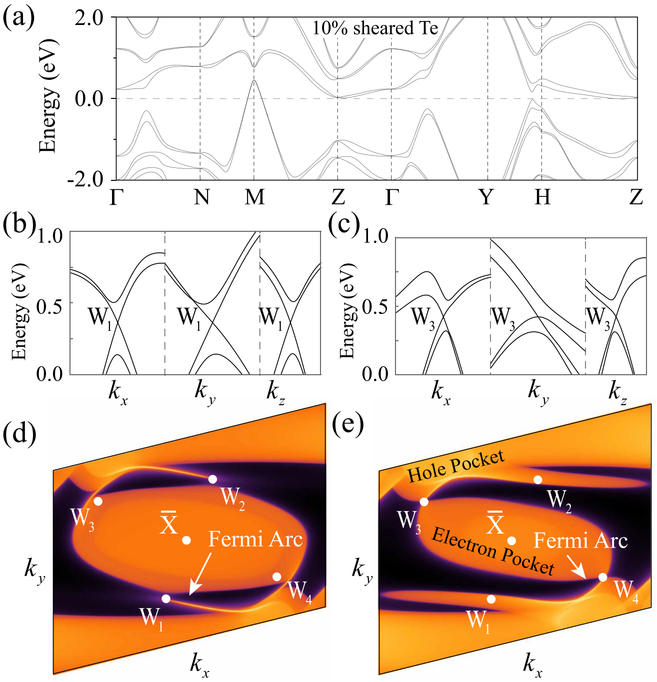

FIG. 3. (a) Band structure of 10% sheared Te. (b), (c) Band dispersions along the k_x, k_y, and k_z directions near the Weyl node (b) W_1 and (c) W_3 of 10% sheared Te. Panel (b) shows a distinct band desperation of type-I Weyl node, while (c) indicates W_3 a type-II Weyl node. (d), (e) Isoenergy band contours for the (001) surface of 10% sheared Te with the Fermi energy fixing at the energy of Weyl node (d) $W_{1,2}$ or (e) $W_{3,4}$. The type-I Weyl node is an isolated point in the surface BZ, while the type-II Weyl node is a point located at the joint of the electron and hole pocket. (d), (e) 0.4 × 0.6 region of surface BZ.

To ensure that the chiralities of Weyl nodes sum to zero in the whole BZ, two Weyl nodes with opposite chirality must exist in the BZ. The two Weyl nodes with chirality +1 are found to be $W_{3,4}$ that locate at ±(0.3673, 0.1782, 0.4306). These four Weyl points are far away from each other, the scattering effect among them is avoided naturally. The first-principles calculations demonstrate that the two pairs of Weyl nodes with opposite chiralities are at slightly different energies: 0.3626 eV for $W_{1,2}$ and 0.4225 eV for $W_{3,4}$, respectively. The slight difference between the energies 0.0559 eV is comparable with that reported in famous type-II WSM $MoTe_2$, i.e., 0.056 eV. Though all of the Weyl nodes are above the Fermi level, they can be experimentally observed by time-resolved photoemission spectroscopy or n-type doping. Meanwhile, see Figs. 3(b) and 3(c), since both the conduction and valance band disperse linearly with a negative slope along k_y near $W_{3,4}$, they are verified to be type-II Weyl nodes, while $W_{1,2}$ are type-I type Weyl nodes. Thus, we realized the minimum Weyl nodes in a system with time-reversal symmetry, i.e., sheared elemental Te.

A general feature of both type-I and -II Weyl nodes is that the characteristic Fermi arcs connecting two Weyl nodes with opposite chiralities appear on the surface. By using MLWF and the Green's function method, to realize the characteristic Fermi arcs, we obtained the isoenergy band contours of 10%

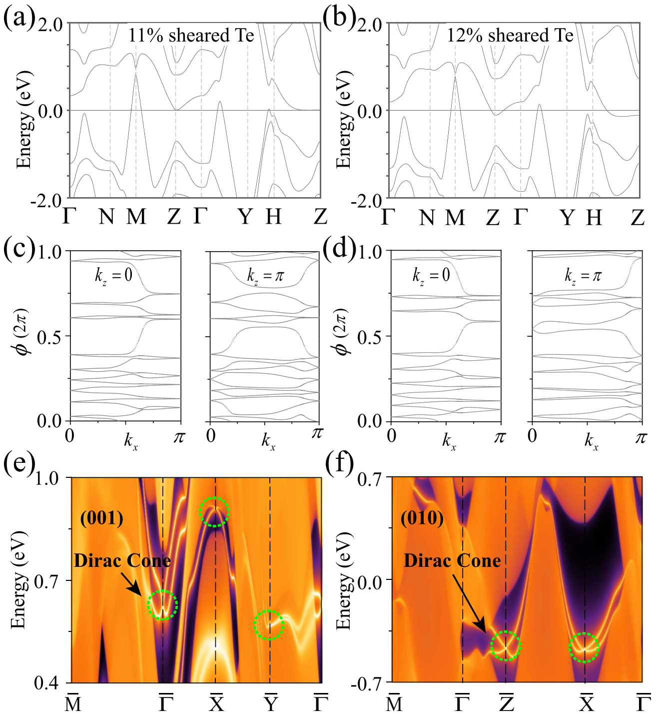

FIG. 4. (a), (b) Band structures of Te under application of (a) 11% and (b) 12% shear strain. There is always a local band gap in both 11% and 12% sheared Te. (c), (d) The Wilson loops of $k_z = 0, \pi$ planes for (c) 11% and (d) 12% sheared Te. (e) The surface state of 11% shear strain for the (001) surface. (f) The surface state of 12% shear strain for the (010) surface. The surface Dirac cones in both (e) and (f) plots are highlighted by the dashes circle in green.

sheared Te for the (001) surface, as shown in Figs. 3(d) and 3(e). Two different types of Weyl nodes perform different features in the isoenergy band contours when projected on the particular surface with Fermi-level fixing to the energy of the node. The project of a type-I Weyl node $\text{W}_{1,2}$ is an isolated point in the band contours, as shown in Fig. 3(d) clearly. Differently, for type-II Weyl nodes, $\text{W}_{3,4}$, the projected point connect the hole and electron pockets, see Fig. 3(e). As shown in Figs. 3(d) and 3(e), besides Fermi arcs connecting $\text{W}_{1,2}$ and $\text{W}_{3,4}$, there is not any other characteristic Fermi arc in the projected BZ, which provides significant evidence of the minimum Weyl nodes in sheared Te.

VI. STI AND WTI PHASES IN SHEARED TE

With stronger shear strain, four Weyl nodes move closer and ultimately annihilate when each pair that carry opposite chiralities get together. In this case, as shown in Fig. 4(a), the system will have local band gap. It is reported that the elemental Te can be induced to a STI phase by shear strain. In sharp contrast, as discussed above, we demonstrate that the Te with slight shear strain is a Weyl semimetal for the appearance of the gapless point in the bulk BZ. Indeed, under application of ≈10.5% shear strain, the four Weyl nodes ultimately annihilate. In this case, elemental Te turns to a system with local gap. The obtained four $\mathbb{Z}_2$ topological invariants $(\nu_0; \nu_1\nu_2\nu_3)$ [78–80] of 11% sheared Te read (1; 010). Due to the absence of inversion symmetry in sheared Te, the $\mathbb{Z}_2$ topological invariants is obtained by the Wilson loop method [81–83]. As shown in Fig. 4(c), there is unavoidable winding in the Wilson loop spectrum in $k_z = 0$ plane, with no winding in that of the $k_z = \pi$ plane. Thus, we have the strong $\mathbb{Z}_2$ topological invariant $\nu_0 = 1$, indicating 11% sheared Te is a STI with local band gap. The surface state of 11% sheared Te for the (001) surface is shown in Fig. 4(e). There are three surface Dirac cones located at the time-reversal invariant momentum $\overline{\Gamma}$, $\overline{\text{X}}$ and $\overline{\text{Y}}$ of surface BZ, which verifies the STI phase.

When we turn the strength of the strain to 12%, the first-principles calculations demonstrate that sheared Te becomes a WTI where the invariants $(\nu_0; \nu_1\nu_2\nu_3)$ read (0; 111). The band structure of 12% sheared Te is shown in Fig. 4(b). The local band gap is observable. Interestingly, as shown in Fig. 4(d), there are Wilson loop windings in the the Wilson loop spectrum in both the $k_z = 0$ and $k_z = \pi$ planes, indicating $\nu_0 = 0$ in this case. To further check the properties of WTI, we compute the surface state of the (010) surface. As shown in Fig. 4(f), there are two surface Dirac cones locating at the $\overline{\text{X}}$ and $\overline{\text{Z}}$ points, respectively. The even number of surface Dirac cones indicate the system turns to a WTI phase indeed [78]. Further calculations show that the system keeps a WTI phase with a larger local gap when 13% shear strain is applied. To the best of our knowledge, there are currently no reports of candidates of WTI phases in the $P1$ (No. 1) space group, where only time-reversal symmetry exists.

VII. THE CWSM PHASE IN SHEARED TE

Since a STI-WTI topological phase transition occurs between the 11% and 12% sheared Te, there must be a band inversion during the process. Thus, it is feasible to find a gapless phase in between the STI and WTI phases. With more careful calculations, a CWSM phase [77] is found under application of ≈11.6% shear strain. One notes that, in the STI-WTI topological phase transition, the topological invariants change from (1; 010) to (0; 111). Thus, the gapless phase must appear near the time-reversal invariant high-symmetry point M : (1/2, 0, 1/2). With the 11.66% shear strain, a CWSM phase with four Weyl nodes is found. The four Weyl nodes are labeled as $\text{W}^c_{1,\cdots,4}$. Specifically, $\text{W}^c_{1,2}$ locate at ±(0.4981, 0.0119, 0.5040) and possess the positive charity. $\text{W}^c_{3,4}$ locate at ±(0.4912, 0.0074, 0.4927) and possess negative charity. Different from the WSM phase in slighter strain (10.0% shear strain as an example) where both type-I and type-II Weyl nodes are found, as shown in Figs. 5(a) and 5(b), all four Weyl nodes in the CWSM phase belong to type-I Weyl nodes. The CWSM phase is characterized by the coexistence of the surface arc and circle in the isoenergy band contours of certain surface bands, which is benefiting from the rich dispersion of the surface states of WSMs [77]. As shown in Figs. 5(c) and 5(d), we can see the surface arc and circle clearly when we fix the Fermi level at the energy of the $\text{W}^c_{1,2}$.

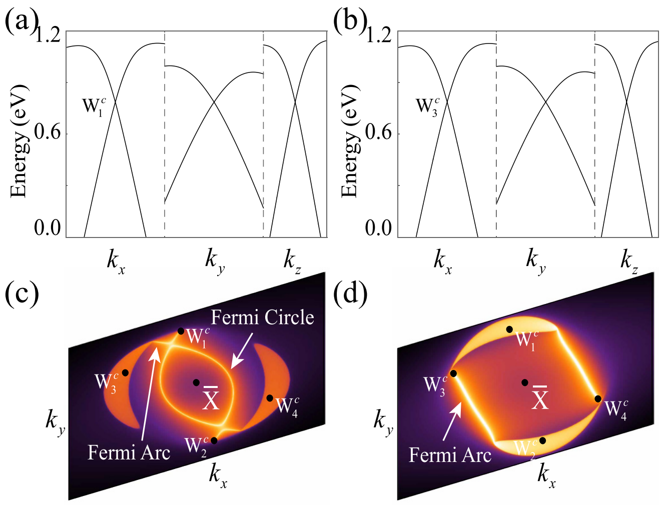

FIG. 5. (a), (b) Band dispersions along the k_x, k_y, and k_z directions near the Weyl nodes (a) W_1^c and (b) W_3^c of 11.66% sheared Te. All four Weyl nodes $W_{1,2,3,4}^c$ belong to type I. (c), (d) The isoenergy band contours for the (001) surface of 11.66% sheared Te with the Fermi energy fixing at the energy of Weyl node (c) $W_{1,2}^c$ or (d) $W_{3,4}^c$. The surface arc and circle coexist in the (001) surface.

VIII. DISCUSSION AND SUMMARY

In summary, by applying shear strain on the noncentrosymmetric elemental Te, we presented a comprehensive investigation on the electronic and topological properties of elemental tellurium. A NI-WSM-STI-CWSM-WTI topological transition and the corresponding topological phase diagram are obtained. The distinct topological properties of different topological nontrivial phases are characterized, respectively. Comparing to previous works, there are many advantages to revealing the nontrivial properties in elemental tellurium: (i) Te has the simplest crystal structure with only one element, which is of great interest in both communities of physics and material science. (ii) In sharp contrast to topological phase transitions revealed in systems with hydrostatic pressure [53,54,84], shear systems with symmetry breaking offer more possibilities for realizing Weyl nodes with a minimum number of nodes. Te has the minimum number of Weyl nodes that can be realized in systems with time reversal symmetry. (iii) The Weyl nodes stay far away from each other, which effectively avoids the interaction between two Weyl nodes. (iv) The WTI phase is found in the space group with the lowest symmetries in real materials. We admit that achieving electronic properties of materials under large strains will be a huge challenge for experimentalists. Fortunately, nontrivial electronic properties in hydrostatic pressure applied Te were reported already [55], giving us confidence in detecting topological phases of sheared strain. Our paper gives systematic recognition of the topological properties of sheared elemental Te and provides a platform to detect the topological phase transition and reveal the deep physics of the topologically nontrivial phases such as exotic transport phenomena induced by the chiral anomaly.

ACKNOWLEDGMENTS

We are grateful to Cheng-Cheng Liu for valuable discussions. This work was supported by the National Natural Science Foundation of China (NSFC, Grants No. 12204074, No. 12222402, No. 11974062, No. 92365101, and No. 12347101) and the Natural Science Foundation of Chongqing (Grant No. CSTB2023NSCQ-JQX0024). D.-S M. also acknowledges funding from the China National Postdoctoral Program for Innovative Talent (Grant No. BX20220367).

[1] X. Wan, A. M. Turner, A. Vishwanath, and S. Y. Savrasov, Topological semimetal and Fermi-arc surface states in the electronic structure of pyrochlore iridates, Phys. Rev. B **83**, 205101 (2011).

[2] A. A. Burkov and L. Balents, Weyl semimetal in a topological insulator multilayer, Phys. Rev. Lett. **107**, 127205 (2011).

[3] H. Weng, C. Fang, Z. Fang, B. A. Bernevig, and X. Dai, Weyl semimetal phase in noncentrosymmetric transition-metal monophosphides, Phys. Rev. X **5**, 011029 (2015).

[4] B. Q. Lv, H. M. Weng, B. B. Fu, X. P. Wang, H. Miao, J. Ma, P. Richard, X. C. Huang, L. X. Zhao, G. F. Chen, Z. Fang, X. Dai, T. Qian, and H. Ding, Experimental discovery of Weyl semimetal TaAs, Phys. Rev. X **5**, 031013 (2015).

[5] A. A. Soluyanov, D. Gresch, Z. Wang, Q. Wu, M. Troyer, X. Dai, and B. A. Bernevig, Type-II Weyl semimetals, Nature (London) **527**, 495 (2015).

[6] A. Burkov, Topological semimetals, Nat. Mater. **15**, 1145 (2016).

[7] B. Yan and C. Felser, Topological materials: Weyl semimetals, Annu. Rev. Condens. Matter Phys. **8**, 337 (2017).

[8] N. P. Armitage, E. J. Mele, and A. Vishwanath, Weyl and Dirac semimetals in three-dimensional solids, Rev. Mod. Phys. **90**, 015001 (2018).

[9] D. Liu, A. Liang, E. Liu, Q. Xu, Y. Li, C. Chen, D. Pei, W. Shi, S. Mo, P. Dudin *et al.*, Magnetic Weyl semimetal phase in a kagomé crystal, Science **365**, 1282 (2019).

[10] B. Q. Lv, T. Qian, and H. Ding, Experimental perspective on three-dimensional topological semimetals, Rev. Mod. Phys. **93**, 025002 (2021).

[11] H. B. Nielsen and M. Ninomiya, Absence of neutrinos on a lattice: (I). Proof by homotopy theory, Nucl. Phys. B **185**, 20 (1981).

[12] H. B. Nielsen and M. Ninomiya, Absence of neutrinos on a lattice: (II). Intuitive topological proof, Nucl. Phys. B **193**, 173 (1981).

[13] R. Wang, B. W. Xia, Z. J. Chen, B. B. Zheng, Y. J. Zhao, and H. Xu, Symmetry-protected topological triangular Weyl complex, Phys. Rev. Lett. **124**, 105303 (2020).

[14] A. C. Potter, I. Kimchi, and A. Vishwanath, Quantum oscillations from surface Fermi arcs in Weyl and Dirac semimetals, Nat. Commun. **5**, 5161 (2014).

[15] S.-Y. Xu, I. Belopolski, N. Alidoust, M. Neupane, G. Bian, C. Zhang, R. Sankar, G. Chang, Z. Yuan, C.-C. Lee *et al.*, Discovery of a Weyl fermion semimetal and topological Fermi arcs, Science **349**, 613 (2015).

[16] Y. Sun, S.-C. Wu, and B. Yan, Topological surface states and Fermi arcs of the noncentrosymmetric Weyl semimetals TaAs, TaP, NbAs, and NbP, Phys. Rev. B **92**, 115428 (2015).

[17] S. Jia, S.-Y. Xu, and M. Z. Hasan, Weyl semimetals, Fermi arcs and chiral anomalies, Nat. Mater. **15**, 1140 (2016).

[18] M. Z. Hasan, S.-Y. Xu, I. Belopolski, and S.-M. Huang, Discovery of Weyl fermion semimetals and topological Fermi arc states, Annu. Rev. Condens. Matter Phys. **8**, 289 (2017).

[19] N. Morali, R. Batabyal, P. K. Nag, E. Liu, Q. Xu, Y. Sun, B. Yan, C. Felser, N. Avraham, and H. Beidenkopf, Fermi-arc diversity on surface terminations of the magnetic Weyl semimetal $Co_3Sn_2S_2$, Science **365**, 1286 (2019).

[20] A. A. Zyuzin and A. A. Burkov, Topological response in Weyl semimetals and the chiral anomaly, Phys. Rev. B **86**, 115133 (2012).

[21] P. Hosur and X. Qi, Recent developments in transport phenomena in Weyl semimetals, C. R. Phys. **14**, 857 (2013).

[22] P. E. C. Ashby and J. P. Carbotte, Chiral anomaly and optical absorption in Weyl semimetals, Phys. Rev. B **89**, 245121 (2014).

[23] D. I. Pikulin, A. Chen, and M. Franz, Chiral anomaly from strain-induced gauge fields in Dirac and Weyl semimetals, Phys. Rev. X **6**, 041021 (2016).

[24] S. Nandy, G. Sharma, A. Taraphder, and S. Tewari, Chiral anomaly as the origin of the planar Hall effect in Weyl semimetals, Phys. Rev. Lett. **119**, 176804 (2017).

[25] D. Vu, W. Zhang, C. Şahin, M. E. Flatté, N. Trivedi, and J. P. Heremans, Thermal chiral anomaly in the magnetic-field-induced ideal Weyl phase of $Bi_{1-x}Sb_x$, Nat. Mater. **20**, 1525 (2021).

[26] X. Huang, L. Zhao, Y. Long, P. Wang, D. Chen, Z. Yang, H. Liang, M. Xue, H. Weng, Z. Fang, X. Dai, and G. Chen, Observation of the chiral-anomaly-induced negative magnetoresistance in 3D Weyl semimetal TaAs, Phys. Rev. X **5**, 031023 (2015).

[27] C.-L. Zhang, S.-Y. Xu, I. Belopolski, Z. Yuan, Z. Lin, B. Tong, G. Bian, N. Alidoust, C.-C. Lee, S.-M. Huang *et al.*, Signatures of the Adler-Bell-Jackiw chiral anomaly in a Weyl fermion semimetal, Nat. Communi. **7**, 10735 (2016).

[28] Y. Wang, E. Liu, H. Liu, Y. Pan, L. Zhang, J. Zeng, Y. Fu, M. Wang, K. Xu, Z. Huang *et al.*, Gate-tunable negative longitudinal magnetoresistance in the predicted type-II Weyl semimetal WTe_2, Nat. Commun. **7**, 13142 (2016).

[29] M. M. Vazifeh and M. Franz, Electromagnetic response of Weyl semimetals, Phys. Rev. Lett. **111**, 027201 (2013).

[30] A. A. Zyuzin and R. P. Tiwari, Intrinsic anomalous hall effect in type-II Weyl semimetals, JETP Lett. **103**, 717 (2016).

[31] E. Liu, Y. Sun, N. Kumar, L. Muechler, A. Sun, L. Jiao, S.-Y. Yang, D. Liu, A. Liang, Q. Xu *et al.*, Giant anomalous Hall effect in a ferromagnetic kagome-lattice semimetal, Nat. Phys. **14**, 1125 (2018).

[32] T. Liang, J. Lin, Q. Gibson, S. Kushwaha, M. Liu, W. Wang, H. Xiong, J. A. Sobota, M. Hashimoto, P. S. Kirchmann *et al.*, Anomalous Hall effect in $ZrTe_5$, Nat. Phys. **14**, 451 (2018).

[33] P. Li, J. Koo, W. Ning, J. Li, L. Miao, L. Min, Y. Zhu, Y. Wang, N. Alem, C.-X. Liu *et al.*, Giant room temperature anomalous Hall effect and tunable topology in a ferromagnetic topological semimetal Co_2MnAl, Nat. Commun. **11**, 3476 (2020).

[34] W. Jiang, D. J. P. de Sousa, J.-P. Wang, and T. Low, Giant anomalous Hall effect due to double-degenerate quasiflat bands, Phys. Rev. Lett. **126**, 106601 (2021).

[35] J. Ruan, S.-K. Jian, D. Zhang, H. Yao, H. Zhang, S.-C. Zhang, and D. Xing, Ideal Weyl semimetals in the chalcopyrites $CuTlSe_2$, $AgTlTe_2$, $AuTlTe_2$, and $ZnPbAs_2$, Phys. Rev. Lett. **116**, 226801 (2016).

[36] J.-R. Soh, F. de Juan, M. G. Vergniory, N. B. M. Schröter, M. C. Rahn, D. Y. Yan, J. Jiang, M. Bristow, P. Reiss, J. N. Blandy, Y. F. Guo, Y. G. Shi, T. K. Kim, A. McCollam, S. H. Simon, Y. Chen, A. I. Coldea, and A. T. Boothroyd, Ideal Weyl semimetal induced by magnetic exchange, Phys. Rev. B **100**, 201102(R) (2019).

[37] L. Yang, Z. Liu, Y. Sun, H. Peng, H. Yang, T. Zhang, B. Zhou, Y. Zhang, Y. Guo, M. Rahn *et al.*, Weyl semimetal phase in the non-centrosymmetric compound TaAs, Nat. Phys. **11**, 728 (2015).

[38] Y. Sun, S.-C. Wu, M. N. Ali, C. Felser, and B. Yan, Prediction of Weyl semimetal in orthorhombic $MoTe_2$, Phys. Rev. B **92**, 161107(R) (2015).

[39] J. Ruan, S.-K. Jian, H. Yao, H. Zhang, S.-C. Zhang, and D. Xing, Symmetry-protected ideal Weyl semimetal in HgTe-class materials, Nat. Commun. **7**, 11136 (2016).

[40] Z. Yu, X. Chen, W. Xia, N. Wang, X. Lv, X. Liu, H. Su, Z. Li, D. Wu, W. Wu *et al.*, Pressure-induced ideal Weyl semimetal state in the layered antiferromagnet $EuCd_2As_2$, arXiv:2202.06016.

[41] A. Bradley, L. The crystal structures of the rhombohedral forms of selenium and tellurium, Philos. Mag. **48**, 477 (1924).

[42] T. Furukawa, Y. Shimokawa, K. Kobayashi, and T. Itou, Observation of current-induced bulk magnetization in elemental tellurium, Nat. Commun. **8**, 954 (2017).

[43] J. Hermann, G. Quentin, and J. Thuillier, Determination of the d_{14} piezoelectric coefficient of tellurium, Solid State Commun. **7**, 161 (1969).

[44] S. K. Ramasesha and A. K. Singh, Thermoelectric power of tellurium under pressure up to 8 GPa, Philos. Mag. B **64**, 559 (1991).

[45] H. Peng, N. Kioussis, and G. J. Snyder, Elemental tellurium as a chiral p-type thermoelectric material, Phys. Rev. B **89**, 195206 (2014).

[46] S. Lin, W. Li, Z. Chen, J. Shen, B. Ge, and Y. Pei, Tellurium as a high-performance elemental thermoelectric, Nat. Commun. **7**, 10287 (2016).

[47] J. Qiao, Y. Pan, F. Yang, C. Wang, Y. Chai, and W. Ji, Few-layer tellurium: One-dimensional-like layered elementary semiconductor with striking physical properties, Sci. Bull. **63**, 159 (2018).

[48] F. Liang and H. Qian, Synthesis of tellurium nanowires and their transport property, Mater. Chem. Phys. **113**, 523 (2009).

[49] E. J. Reed, Two-dimensional tellurium, Nature (London) **552**, 40 (2017).

[50] Z. Zhu, X. Cai, S. Yi, J. Chen, Y. Dai, C. Niu, Z. Guo, M. Xie, F. Liu, J.-H. Cho, Y. Jia, and Z. Zhang, Multivalency-driven formation of Te-based monolayer materials: A combined first-principles and experimental study, Phys. Rev. Lett. **119**, 106101 (2017).

[51] Z. Shi, R. Cao, K. Khan, A. K. Tareen, X. Liu, W. Liang, Y. Zhang, C. Ma, Z. Guo, X. Luo *et al.*, Two-dimensional tellurium: Progress, challenges, and prospects, Nano-Micro Letters **12**, 1 (2020).

[52] V. Selamneni, T. Akshaya, V. Adepu, and P. Sahatiya, Laser-assisted micropyramid patterned PDMS encapsulation of 1D tellurium nanowires on cellulose paper for highly sensitive

strain sensor and its photodetection studies, Nanotechnology **32**, 455201 (2021).

[53] L. A. Agapito, N. Kioussis, W. A. Goddard, and N. P. Ong, Novel family of chiral-based topological insulators: Elemental tellurium under strain, Phys. Rev. Lett. **110**, 176401 (2013).

[54] M. Hirayama, R. Okugawa, S. Ishibashi, S. Murakami, and T. Miyake, Weyl node and spin texture in trigonal eellurium and selenium, Phys. Rev. Lett. **114**, 206401 (2015).

[55] T. Ideue, M. Hirayama, H. Taiko, T. Takahashi, M. Murase, T. Miyake, S. Murakami, T. Sasagawa, and Y. Iwasa, Pressure-induced topological phase transition in noncentrosymmetric elemental tellurium, Proc. Natl. Acad. Sci. USA **116**, 25530 (2019).

[56] D. Rodriguez, A. A. Tsirlin, T. Biesner, T. Ueno, T. Takahashi, K. Kobayashi, M. Dressel, and E. Uykur, Two linear regimes in optical conductivity of a Type-I Weyl semimetal: The case of elemental tellurium, Phys. Rev. Lett. **124**, 136402 (2020).

[57] K. Nakayama, M. Kuno, K. Yamauchi, S. Souma, K. Sugawara, T. Oguchi, T. Sato, and T. Takahashi, Band splitting and Weyl nodes in trigonal tellurium studied by angle-resolved photoemission spectroscopy and density functional theory, Phys. Rev. B **95**, 125204 (2017).

[58] G. Gatti, D. Gosálbez-Martínez, S. S. Tsirkin, M. Fanciulli, M. Puppin, S. Polishchuk, S. Moser, L. Testa, E. Martino, S. Roth, P. Bugnon, L. Moreschini, A. Bostwick, C. Jozwiak, E. Rotenberg, G. Di Santo, L. Petaccia, I. Vobornik, J. Fujii, J. Wong *et al.*, Radial spin texture of the Weyl fermions in chiral tellurium, Phys. Rev. Lett. **125**, 216402 (2020).

[59] M. Sakano, M. Hirayama, T. Takahashi, S. Akebi, M. Nakayama, K. Kuroda, K. Taguchi, T. Yoshikawa, K. Miyamoto, T. Okuda, K. Ono, H. Kumigashira, T. Ideue, Y. Iwasa, N. Mitsuishi, K. Ishizaka, S. Shin, T. Miyake, S. Murakami, T. Sasagawa *et al.*, Radial spin texture in elemental tellurium with chiral crystal structure, Phys. Rev. Lett. **124**, 136404 (2020).

[60] S. Murakami, Phase transition between the quantum spin Hall and insulator phases in 3D: Emergence of a topological gapless phase, New J. Phys. **9**, 356 (2007).

[61] P. Hohenberg and W. Kohn, Inhomogeneous electron gas, Phys. Rev. **136**, B864 (1964).

[62] W. Kohn and L. J. Sham, Self-consistent equations including exchange and correlation effects, Phys. Rev. **140**, A1133 (1965).

[63] G. Kresse and D. Joubert, From ultrasoft pseudopotentials to the projector augmented-wave method, Phys. Rev. B **59**, 1758 (1999).

[64] P. E. Blöchl, Projector augmented-wave method, Phys. Rev. B **50**, 17953 (1994).

[65] G. Kresse and J. Furthmüller, Efficiency of ab-initio total energy calculations for metals and semiconductors using a plane-wave basis set, Comput. Mater. Sci. **6**, 15 (1996).

[66] G. Kresse and J. Furthmüller, Efficient iterative schemes for *ab initio* total-energy calculations using a plane-wave basis set, Phys. Rev. B **54**, 11169 (1996).

[67] J. Heyd, G. E. Scuseria, and M. Ernzerhof, Hybrid functionals based on a screened coulomb potential, J. Chem. Phys. **118**, 8207 (2003).

[68] R. Keller, W. B. Holzapfel, and H. Schulz, Effect of pressure on the atom positions in Se and Te, Phys. Rev. B **16**, 4404 (1977).

[69] N. Marzari and D. Vanderbilt, Maximally localized generalized Wannier functions for composite energy bands, Phys. Rev. B **56**, 12847 (1997).

[70] I. Souza, N. Marzari, and D. Vanderbilt, Maximally localized Wannier functions for entangled energy bands, Phys. Rev. B **65**, 035109 (2001).

[71] A. A. Mostofi, J. R. Yates, Y.-S. Lee, I. Souza, D. Vanderbilt, and N. Marzari, wannier90: A tool for obtaining maximally-localised Wannier functions, Comput. Phys. Commun. **178**, 685 (2008).

[72] N. Marzari, A. A. Mostofi, J. R. Yates, I. Souza, and D. Vanderbilt, Maximally localized Wannier functions: Theory and applications, Rev. Mod. Phys. **84**, 1419 (2012).

[73] A. A. Mostofi, J. R. Yates, G. Pizzi, Y.-S. Lee, I. Souza, D. Vanderbilt, and N. Marzari, An updated version of wannier90: A tool for obtaining maximally-localised Wannier functions, Comput. Phys. Commun. **185**, 2309 (2014).

[74] Q. Wu, S. Zhang, H.-F. Song, M. Troyer, and A. A. Soluyanov, Wanniertools: An open-source software package for novel topological materials, Comput. Phys. Commun. **224**, 405 (2018).

[75] V. Anzin, M. Eremets, Y. V. Kosichkin, A. Nadezhdinskii, and A. Shirokov, Measurement of the energy gap in tellurium under pressure, Phys. Status Solidi (A) **42**, 385 (1977).

[76] R. S. Caldwell and H. Fan, Optical properties of tellurium and selenium, Phys. Rev. **114**, 664 (1959).

[77] C.-C. Liu, J.-J. Zhou, Y. Yao, and F. Zhang, Weak topological insulators and composite Weyl semimetals: β-Bi$_4X_4$ (X = Br, I), Phys. Rev. Lett. **116**, 066801 (2016).

[78] L. Fu, C. L. Kane, and E. J. Mele, Topological insulators in three dimensions, Phys. Rev. Lett. **98**, 106803 (2007).

[79] R. Roy, Topological phases and the quantum spin Hall effect in three dimensions, Phys. Rev. B **79**, 195322 (2009).

[80] J. E. Moore and L. Balents, Topological invariants of time-reversal-invariant band structures, Phys. Rev. B **75**, 121306(R) (2007).

[81] A. A. Soluyanov and D. Vanderbilt, Computing topological invariants without inversion symmetry, Phys. Rev. B **83**, 235401 (2011).

[82] R. Yu, X. L. Qi, A. Bernevig, Z. Fang, and X. Dai, Equivalent expression of $\mathbb{Z}_2$ topological invariant for band insulators using the non-Abelian Berry connection, Phys. Rev. B **84**, 075119 (2011).

[83] H. Weng, R. Yu, X. Hu, X. Dai, and Z. Fang, Quantum anomalous Hall effect and related topological electronic states, Adv. Phys. **64**, 227 (2015).

[84] J. Liu, Y. Xu, J. Wu, B.-L. Gu, S. Zhang, and W. Duan, Manipulating topological phase transition by strain, Acta Crystallogr. C: Struct. Chem. **70**, 118 (2014).